

# PROBING PRE-GALACTIC METAL ENRICHMENT WITH HIGH-REDSHIFT GAMMA-RAY BURSTS

F. Y. WANG<sup>1,2,7</sup>, VOLKER BROMM<sup>2,3</sup>, THOMAS H. GREIF<sup>4</sup>, ATHENA STACY<sup>5</sup>, Z. G. DAI<sup>1</sup>, ABRAHAM LOEB<sup>6</sup> AND K. S. CHENG<sup>7</sup>

<sup>1</sup>School of Astronomy and Space Science, Nanjing University, Nanjing 210093, China

<sup>2</sup>Department of Astronomy, University of Texas at Austin, Austin, TX 78712, USA

<sup>3</sup>Texas Cosmology Center, University of Texas at Austin, TX 78712, USA

<sup>4</sup>Max-Planck-Institut für Astrophysik, Karl-Schwarzschild-Strasse 1, 85740 Garching bei München, Germany

<sup>5</sup>NASA Goddard Space Flight Center, Greenbelt, MD 20771, USA

<sup>6</sup>Astronomy Department, Harvard University, 60 Garden St., Cambridge, MA 02138, USA

<sup>7</sup>Department of Physics, The University of Hong Kong, Pokfulam Road, Hong Kong, China

*Draft version October 16, 2018*

## ABSTRACT

We explore high-redshift gamma-ray bursts (GRBs) as promising tools to probe pre-galactic metal enrichment. We utilize the bright afterglow of a Population III (Pop III) GRB exploding in a primordial dwarf galaxy as a luminous background source, and calculate the strength of metal absorption lines that are imprinted by the first heavy elements in the intergalactic medium (IGM). To derive the GRB absorption line diagnostics, we use an existing highly-resolved simulation of the formation of a first galaxy which is characterized by the onset of atomic hydrogen cooling in a halo with virial temperature  $\gtrsim 10^4$  K. We explore the unusual circumburst environment inside the systems that hosted Pop III stars, modeling the density evolution with the self-similar solution for a champagne flow. For minihalos close to the cooling threshold, the circumburst density is roughly proportional to  $(1+z)$  with values of about a few  $\text{cm}^{-3}$ . In more massive halos, corresponding to the first galaxies, the density may be larger,  $n \gtrsim 100 \text{ cm}^{-3}$ . The resulting afterglow fluxes are weakly dependent on redshift at a fixed observed time, and may be detectable with the *James Webb Space Telescope (JWST)* and Very Large Array (VLA) in the near-IR and radio wavebands, respectively, out to redshift  $z \gtrsim 20$ . We predict that the maximum of the afterglow emission shifts from near-IR to millimeter bands with peak fluxes from mJy to Jy at different observed times. The metal absorption line signature is expected to be detectable in the near future. GRBs are ideal tools for probing the metal enrichment in the early IGM, due to their high luminosities and featureless power-law spectra. The metals in the first galaxies produced by the first supernova (SN) explosions are likely to reside in low-ionization stages (C II, O I, Si II and Fe II). We show that if the afterglow can be observed sufficiently early, analysis of the metal lines may distinguish whether the first heavy elements were produced in a pair-instability supernova (PISN), or a core-collapse (Type II) SN, thus constraining the initial mass function of the first stars.

*Subject headings:* cosmology: observations – cosmology: theory – galaxies: high-redshift – gamma rays: bursts – quasars: absorption lines

## 1. INTRODUCTION

One of the key goals in modern cosmology is to study the formation of the first stars and galaxies at the end of the cosmic dark ages, and how they shaped the subsequent evolution of the universe (Barkana & Loeb 2001; Bromm & Larson 2004; Ciardi & Ferrara 2005; Bromm et al. 2009; Loeb 2010). The first, so-called Population III (Pop III) stars are predicted to have formed at  $z \gtrsim 20$  in minihalos with virial mass  $M_{\text{vir}} \sim 10^6 M_{\odot}$  and temperatures  $T_{\text{vir}} < 10^4$  K (Haiman et al. 1996; Tegmark et al. 1997; Yoshida et al. 2003). The Pop III initial mass function (IMF) is thought to be top-heavy (Bromm et al. 1999, 2002; Abel et al. 2002), possibly extending to  $M_* \gtrsim 100 M_{\odot}$ , but recent simulations indicate that the Pop III IMF may be quite broad, also including a fraction of lower-mass stars (Stacy et al. 2010; Clark et al. 2011b; Greif et al. 2011, 2012). The first bona-fide galaxies are expected to have formed at a later stage in hierarchical structure formation (Bromm & Yoshida 2011), when  $\sim 10^8 M_{\odot}$  halos assembled at  $z \gtrsim 10$  via the merging of progenitor minihalos (Wise & Abel 2007; Greif et al.

2008). These systems are often termed ‘atomic cooling halos’, because their virial temperature,  $T_{\text{vir}} \gtrsim 10^4$  K, exceeds the threshold to enable efficient cooling via lines of atomic hydrogen (Oh & Haiman 2002). Direct observations of the first galaxies at redshifts  $z > 10$  have so far been out of reach. In the coming decade, the *James Webb Space Telescope (JWST)* promises to directly probe this critical period (Gardner et al. 2006). The detection of metal absorption lines in the afterglow spectrum of high-redshift gamma-ray bursts (GRBs), imprinted by enriched gas in the first galaxies, offers an unusual opportunity to study the physical conditions inside them. We may thus be able to derive constraints on the temperature, metallicity, ionization state, and kinematics in the interstellar medium (ISM) of high-redshift galaxies, and in the surrounding intergalactic medium (IGM). It is encouraging that such diagnostics can already be obtained for bursts at somewhat lower redshifts. An example is GRB 081008, where high-resolution spectroscopy with the VLT has probed the ISM of a host galaxy at  $z \simeq 2$  (D’Elia et al. 2011).

Long-duration GRBs have been shown to be associ-

ated with the death of massive stars (Stanek et al. 2003; Hjorth et al. 2003; Woosley & Bloom 2006). Their high luminosities make them detectable out to the edge of the visible universe (Ciardi & Loeb 2000; Lamb & Reichart 2000; Bromm & Loeb 2002, 2006; Gou et al. 2004; Inoue et al. 2007; Mészáros & Rees 2010), with the current record held by GRB 090429B at  $z \sim 9.4$  (Cucchiara et al. 2011). GRBs provide ideal probes of the high-redshift universe, including the star formation rate (Totani 1997; Wijers et al. 1998; Porciani & Madau 2001; Chary et al. 2007; Yüksel et al. 2008; Wang & Dai 2009, 2011; Elliott et al. 2012), reionization (Gallerani et al. 2008), dark energy (Dai et al. 2004; Wang et al. 2011), and the IGM metal enrichment (Barkana & Loeb 2004; Totani et al. 2006; Toma et al. 2011; Bromm & Loeb 2012). The leading contender for the central engine of long-duration GRBs is the collapsar model (Woosley 1993; MacFadyen et al. 2001). Because of their predicted high characteristic mass, a significant fraction of Pop III stars might end their lives as a black hole, potentially leading to a large number of high-redshift GRBs. Thus, Pop III stars are viable progenitors of long-duration GRBs, triggered by the collapsar mechanism, as long as they can lose their outer envelope and retain sufficient angular momentum in their center (Bromm & Loeb 2006; Belczynski et al. 2007; Komissarov & Barkov 2010; Stacy et al. 2011). It might even be possible for Pop III collapsars to occur if the extended outer envelope were not lost (Suwa & Ioka 2011).

The history of pre-galactic metal enrichment has several important consequences for structure formation (Madau et al. 2001; Karlsson et al. 2012). An early phase of metal injection may qualitatively change the character of star formation, from a predominantly high-mass (Pop III) mode to a normal, low-mass dominated (Pop I/II) one, once the enrichment has exceeded a ‘critical metallicity’ of  $Z_{\text{crit}} \sim 10^{-4} Z_{\odot}$  (Bromm et al. 2001a; Schneider et al. 2002, 2006; Bromm & Loeb 2003; Mackey et al. 2003). The transition between these two modes has crucial implications, e.g., for the expected redshift distribution of GRBs (Bromm & Loeb 2006; Campisi et al. 2011; de Souza et al. 2011), for reionization (Cen 2003; Wyithe & Loeb 2003; Furlanetto & Loeb 2005), and for the chemical abundance patterns of low-metallicity stars (Qian & Wasserburg 2001; Frebel et al. 2007, 2009; Tumlinson 2010). It is therefore important to explore the topology of early metal enrichment, and to determine when particular regions in the universe become supercritical (Tornatore et al. 2007; Maio et al. 2010).

Absorption lines imprinted on the spectra of bright background sources, such as GRBs or quasars, are one of the main sources of information about the physical and chemical properties of high-redshift systems (Oh 2002; Furlanetto & Loeb 2003; Oppenheimer et al. 2009). These lines are due mainly to absorption by neutral hydrogen present in the low column-density Ly $\alpha$  forest, and by metals in low-ionization stages (e.g., C II, Si II, Mg II, Fe II, O I) which arise in the higher column-density gas associated with Damped Ly $\alpha$  Absorbers (DLAs). The analysis of the spectrum of distant GRB 050904 (Totani et al. 2006) has resulted in a wealth of detailed insight into the physical conditions within the host galaxy at

$z \simeq 6.3$ , and Salvaterra et al. (2009) claimed that they identified two absorption lines (Si IV and Fe II), although at poor signal-to-noise, in the spectrum of GRB 090423, the most distant spectroscopically confirmed burst at  $z = 8.2$  (Salvaterra et al. 2009; Tanvir et al. 2009). GRBs as background sources offer a number of advantages compared to traditional lighthouses such as quasars (Bromm & Loeb 2012). Their number density drops much less precipitously than quasars at  $z > 6$  (Fan et al. 2006), and the absence of a strong proximity effect, together with the near power-law character of their spectra, renders them ideal probes of the early IGM.

In this paper, we discuss the observational signatures of Pop III GRBs and study pre-galactic metal enrichment utilizing absorption lines in the spectra of high- $z$  GRBs which were imprinted by the first galaxies. Recently, it has become feasible to study the formation of the first galaxies, including the metal enrichment from Pop III supernovae (SNe), with highly-resolved cosmological simulations (Wise & Abel 2008; Greif et al. 2010). We here place a bright GRB into the simulation box of Greif et al. (2010), and derive the spectral signature as the afterglow light escapes from the first galaxy, thereby probing the partially enriched IGM in its vicinity. The fluxes in the near-IR and radio bands may be detectable by the *JWST* and the Very Large Array (VLA) out to  $z \gtrsim 20$ . The structure of this paper is as follows. In Section 2, we derive the circumburst density profile of Pop III GRBs, followed by a brief description of the underlying first galaxy simulation (Section 3). We discuss the properties of the GRB afterglow in Section 4, and the metal absorption line diagnostics in Section 5, followed by our conclusions.

## 2. GRB DENSITY PROFILE

Two different environments are currently discussed as Pop III star formation sites, minihalos and atomic cooling halos (Bromm et al. 2009). The latter mode is often termed Pop III.2 to indicate physical conditions, such as a higher degree of ionization, that differs from the canonical minihalo case, possibly resulting in somewhat lower masses (McKee & Tan 2008). For normal GRBs, either a constant number-density profile, or a power-law dependence, as might be expected in the stellar wind from the progenitor, is discussed in the literature (Bloom 2011). The GRB afterglow emission sensitively depends on the circumburst density (Ciardi & Loeb 2000; Gou et al. 2004; Inoue et al. 2007), and this is one of the crucial uncertainties in making predictions for Pop III bursts. We next derive the likely circumburst conditions in the two possible Pop III host systems.

### 2.1. Minihalo case

For simplicity, we assume that Pop III GRBs are triggered in minihalos close to the cooling threshold for collapse, which is only weakly dependent on redshift (Yoshida et al. 2003). For definiteness, we choose  $M_{\text{vir}} \simeq 10^6 M_{\odot}$ . To determine the pre-burst density, we need to consider the build-up of the H II region around the central Pop III star, and how the density structure is modified through the strong photoionization-heating inside of it (Whalen et al. 2004). The production of ionizing photons strongly depends on the stellar mass, which in turn is determined by how the accretion flow onto the

growing protostar proceeds under the influence of this radiation field (e.g., McKee & Tan 2008; Hosokawa et al. 2011; Smith et al. 2011; Stacy et al. 2012). Thus, the assembly of Pop III stars and the development of an H II region around them proceed simultaneously and affect each other. The shallow potential wells in the host minihalos, with corresponding circular velocities of a few  $\text{km s}^{-1}$ , are unable to retain photo-ionized gas, so that the gas is effectively blown out of the minihalo. The resulting photo-evaporation has been studied with 3D radiative transfer calculations (Alvarez et al. 2006; Abel et al. 2007; Greif et al. 2009), where one massive Pop III star at the center of the minihalo acts as an embedded point source, that also take into account the hydrodynamic response of the photo-heated gas.

It is possible to understand the key physics of the photoevaporation from minihalos with the self-similar solution for a champagne flow (Shu et al. 2002). Assuming a  $\rho \propto r^{-2}$  density profile, which describes the typical situation in minihalos outside a nearly flat inner core, one can reformulate the spherically symmetric continuity and Euler equations for isothermal gas as follows:

$$[(v-x)^2 - 1] \frac{1}{\alpha} \frac{d\alpha}{dx} = \left[ \alpha - \frac{2}{x}(x-v) \right] (x-v), \quad (1)$$

$$[(v-x)^2 - 1] \frac{dv}{dx} = \left[ (x-v)\alpha - \frac{2}{x} \right] (x-v), \quad (2)$$

where  $x = r/c_s t$  is the similarity variable, and  $\rho(r, t) = \alpha(x)/4\pi G t^2 = m_H n(r)/X$  and  $u(r, t) = c_s v(x)$  introduce the reduced density and velocity, respectively.  $c_s$  is the sound speed of the ionized gas and  $X = 0.75$  the hydrogen mass fraction. The density globally decreases with time, after the ionizing source has turned on. To derive the immediate pre-explosion value, we will therefore set  $t = t_* \simeq 3 \times 10^6$  yr, the typical lifetime of a massive Pop III star (e.g., Bromm et al. 2001b).

Different solutions are obtained depending on the ratio  $\epsilon \equiv (c_{s,i}/c_s)^2$ , where  $c_{s,i}$  and  $c_s$  are the initial and ionized isothermal sound speeds. We take  $T = 3 \times 10^4$  K and  $T_i = T_{\text{vir}}$ , where the virial temperature is defined as

$$T_{\text{vir}} \simeq \frac{GM_{\text{vir}} m_H}{2R_{\text{vir}} k_B} \simeq 10^4 \text{ K} \left( \frac{M}{10^8 M_\odot} \right)^{2/3} \left( \frac{1+z}{10} \right). \quad (3)$$

The intuition behind the latter identification is that  $c_{s,i}^2 \simeq k_B T_{\text{vir}}/m_H \simeq v_{\text{vir}}^2$ , the specific gravitational potential energy of the gas inside a halo, is a measure of how strongly the fluid is bottled up, before a champagne flow can occur. Using table 1 in Shu et al. (2002), we can obtain the density profiles at different redshifts as follow. First, the value of  $\epsilon$  can be calculated at the given redshift. We then derive the corresponding reduced central density,  $\alpha_0$ , via interpolation. For the given  $\alpha_0$  we can numerically solve equations (1) and (2) subject to the inner boundary conditions:

$$\alpha = \alpha_0 \quad \text{and} \quad v = 0, \quad \text{at} \quad x = 0. \quad (4)$$

To avoid the singularity near  $x = 0$ , Shu et al. (2002) provide the series expansion

$$\alpha = \alpha_0 + \frac{\alpha_0}{6} \left( \frac{2}{3} - \alpha_0 \right) x^2 + \dots, \quad (5)$$

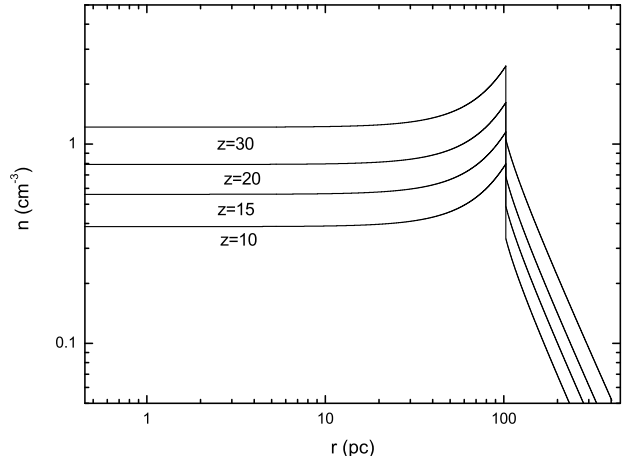


FIG. 1.— Minihalo circumburst environment. Shown is the hydrogen number density vs. distance from the central Pop III star at the moment of its death, 3 Myr after it was born. The density profiles are given by the Shu solution for different redshifts, as labelled. Typical circumburst densities are  $\sim 1 \text{ cm}^{-3}$ , with smaller values at lower redshifts. The redshift trend reflects the shallower minihalo potential wells at later times.

$$v = \frac{2}{3}x + \frac{1}{45} \left( \frac{2}{3} - \alpha_0 \right) x^3 + \dots \quad (6)$$

Once the Pop III star has turned on at  $t = 0$ , the photoheating commences, putting in place a pressurized inner bubble which leads to an outward-flowing shock at  $x_{\text{sh}}$ . The shock obeys the usual isothermal jump conditions, written in terms of the reduced variables as

$$(v_u - x_{\text{sh}})(v_d - x_{\text{sh}}) = 1, \quad \frac{\alpha_d}{\alpha_u} = (v_u - x_{\text{sh}})^2, \quad (7)$$

where the subscript  $u(d)$  indicates the value of the reduced velocity and density upstream (downstream) of the shock.

In Figure 1, we show the resulting density profiles at the end of the Pop III progenitor's life, and therefore at the completion of the photoionization-heating as well. As can be seen, the circumstellar densities have dropped significantly from the high values,  $\gtrsim 10^4 \text{ cm}^{-3}$ , present prior to Pop III star formation, and are nearly uniform at small radii. Such a flat density profile is markedly different from that created by stellar winds. The absence of any wind around a Pop III star is indeed predicted, as a consequence of very low metallicity (Baraffe et al. 2001; Kudritzki 2002), and could serve as an indicator of a low- $Z$  GRB progenitor. The post-photoheating density evolves with redshift, approximately according to  $n_{\text{pi}} \propto (1+z)$ , normalized such that  $n \simeq 1 \text{ cm}^{-3}$  at  $z \simeq 20$ . This law differs from earlier estimates of the Pop III circumburst evolution, where no  $z$ -dependence was assumed, or a scaling with the density of the background universe,  $n_{\text{pi}} \propto (1+z)^3$  (e.g., Gou et al. 2004).

This relation can be understood as follows. Prior to the onset of protostellar collapse, the baryonic density profile in the minihalo can be described by the Lane-Emden equation for an isothermal sphere

$$\frac{1}{r^2} \frac{d}{dr} \left( r^2 \frac{d\phi}{dr} \right) = 4\pi G \rho_0 e^{-\phi/a^2}, \quad (8)$$

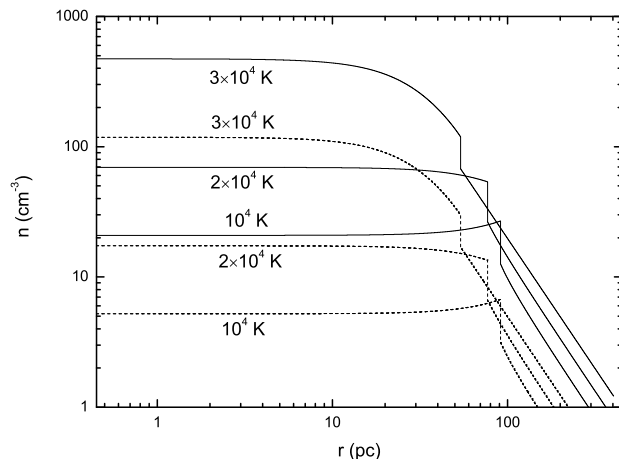


FIG. 2.— Atomic-cooling-halo circumburst environment. The density profiles are again calculated from the Shu solution, evaluated at  $t = 3 \times 10^6$  yr after source turn-on. The collapse redshift is here indirectly given by the virial temperature, as labelled. We show the case of photoheating from only a single Pop III star (*solid lines*), and that from a stellar cluster (*dotted lines*). The resulting densities again exhibit a nearly uniform inner core, but overall values are much higher than in the minihalo case (see Fig. 1).

where  $\rho_0$  is the density at which the gravitational potential  $\phi$  is set to zero. A simple analytical solution to this equation is the well-known singular isothermal sphere (SIS):  $\rho_{\text{SIS}} = a^2/(2\pi Gr^2)$ , where  $a^2 \simeq k_B T_{\text{vir}}/m_H$ . This law approximately describes the profile found in realistic simulations of first star formation (e.g., Yoshida et al. 2003), outside an inner core of radius  $r_J \sim 1$  pc, the Jeans length of the primordial gas (Bromm et al. 2002). The baryonic mass inside the shock radius,  $r_{\text{sh}} = c_s t_* \simeq 100$  pc, is about

$$M_i = \int_{r_J}^{r_{\text{sh}}} 4\pi r^2 \rho_{\text{SIS}}(z, r) dr. \quad (9)$$

At the end of photoionization-heating, the mass in the flat inner core is about

$$M_f = \frac{4\pi}{3} r_{\text{sh}}^3 \rho_{\text{pi}} = \frac{4\pi}{3} r_{\text{sh}}^3 n_{\text{pi}} m_H X. \quad (10)$$

If we neglect any outflows at large radii, we have approximate mass conservation, such that  $M_i \simeq M_f$ , resulting in  $n_{\text{pi}} \propto T_{\text{vir}} \propto (1+z)$ , as before.

Our post-photoheating densities are consistent with simulation results (Kitayama et al. 2004; Alvarez et al. 2006; Abel et al. 2007; Greif et al. 2009, 2010). We also agree with Whalen et al. (2004), if we take into account that their halo had a somewhat lower mass,  $M_{\text{vir}} \simeq 5 \times 10^5 M_\odot$ . Empirical support is provided in Chandra et al. (2010) who found that the circumburst density of GRB 090423 at  $z = 8.2$  was about  $n \sim 0.9 \text{ cm}^{-3}$  by fitting the radio, X-ray and infrared afterglow, although this burst almost certainly did not originate in a minihalo environment.

## 2.2. Atomic cooling halo case

Star formation and radiative feedback inside atomic cooling halos is significantly less well-understood than

the minihalo case (e.g., Johnson et al. 2009; Safranek-Shrader et al. 2010, 2012), and there are no comparable high-resolution simulations yet. What is the character of star formation, in terms of IMF and stellar multiplicity (Clark et al. 2011a)? Given current uncertainty, we here again use the formalism of the Shu solution as developed above. We further assume for simplicity that either a single Pop III star forms, or a small stellar cluster, with properties that would again heat the surrounding H II region to  $T \simeq 3 \times 10^4$  K. We stress that the numbers derived here only provide us with rough guesses at best, and the hope is that simulations will eventually become available to firm them up.

If a cluster of Pop III stars forms, the time where photoheating stops will be prolonged. We thus need to evaluate  $\rho(r, t) = \alpha(x)/4\pi G t^2$  at  $t = t_{\text{cluster}} \simeq t_* + t_{\text{SF}}$ , where  $t_{\text{SF}}$  is the timescale over which star formation is ongoing, and  $t_*$  again is the lifetime of a single Pop III star. We can estimate  $t_{\text{SF}} \sim t_*$ , because disruptive feedback effects will tend to terminate star formation when the first member stars die. The resulting densities at the end of photoheating are shown in Figure 2. Similar to the minihalo case, densities are nearly constant at small radii, but overall values are much higher. The reason is that here the potential wells are deeper, so that photoheated gas can more easily be retained. Typical circumburst densities are  $n_{\text{pi}} \sim 100 \text{ cm}^{-3}$ . Because such large densities would correspond to high afterglow fluxes, Pop III GRBs originating in atomic cooling halos may be extremely bright, rendering them visible out to very high redshifts. For some of the most distant bursts known, such large circumburst densities have indeed been inferred. E.g., Gou et al. (2007) have argued that fitting the GRB 050904 afterglow at  $z = 6.3$  requires a circumburst density of a few  $100 \text{ cm}^{-3}$ . Similar values have been suggested for GRB 080913 at  $z = 6.7$  (Greiner et al. 2009; Zhang et al. 2009).

## 3. MODELING PRE-GALACTIC ENRICHMENT

In order to predict afterglow spectra from Pop III GRBs, we consider explosions that are embedded in a realistic cosmological setting. Specifically, we use the first galaxy simulation carried out by Greif et al. (2010), where the assembly of an atomic cooling halo was tracked, resolving all prior Pop III star formation in the progenitor minihalos, together with the radiative feedback from H II regions around those stars. In addition, the simulation allowed one of the Pop III progenitor stars to explode as an energetic SN, explicitly following the transport and mixing of the ejected metals into the IGM. We here summarize a few key aspects of the simulation, and refer the reader to Greif et al. (2010) for further details.

The simulation is carried out in a cosmological box of size 1 Mpc (comoving), and is initialized at  $z = 99$  according to a concordance  $\Lambda$  cold dark matter ( $\Lambda$ CDM) model with matter density  $\Omega_m = 1 - \Omega_\Lambda = 0.3$ , baryon density  $\Omega_b = 0.04$ , Hubble parameter  $h = H_0/(100 \text{ km s}^{-1} \text{ Mpc}^{-1}) = 0.7$ , spectral index  $n_s = 1.0$ , and normalization  $\sigma_8 = 0.9$  (Spergel et al. 2003). Density and velocity perturbations are imprinted at recombination with a Gaussian distribution, and they are propagated to  $z = 99$ , when the simulation is started, by applying the Zeldovich approximation. Within the highest res-

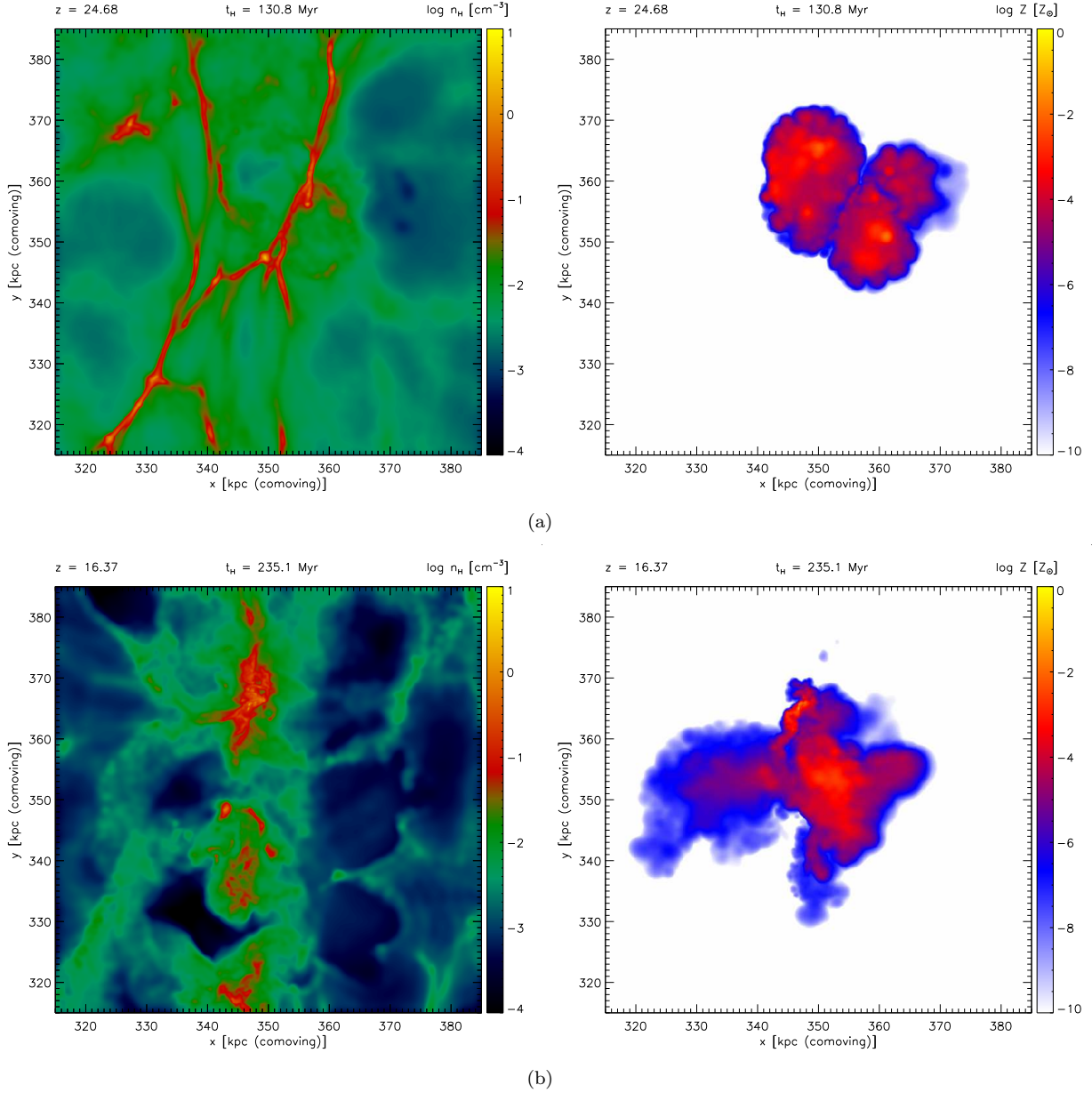


FIG. 3.— Possible explosion sites for high- $z$  GRBs. Shown are the hydrogen number density and metallicity contours during the assembly of a first galaxy, averaged along the line of sight within the central  $\simeq 100$  kpc (comoving), at two different redshifts. *Panel (a)*:  $z \simeq 25$ , briefly after the first Pop III SN exploded. At this time, most of the metals reside in the IGM. *Panel (b)*:  $z \simeq 16.4$ , closer to the virialization of the atomic cooling halo. Now, metals are being re-assembled into the growing potential well of the first galaxy. The topology of metal enrichment is highly inhomogeneous, with pockets of highly enriched material embedded in regions with a largely primordial composition. These plots are derived from the simulation described in Greif et al. (2010).

olution region of our nested, zoomed-in initial conditions, the DM and gas particle masses are  $33M_\odot$  and  $5M_\odot$ , respectively. The baryonic mass resolution, roughly given by the mass contained inside an SPH kernel, is  $\simeq 400M_\odot$ , close to the relevant Jeans mass in the primordial star-forming gas. To capture the chemical evolution of the gas, the simulation follows the abundances of H,  $H^+$ ,  $H^-$ ,  $H_2$ ,  $H_2^+$ , He,  $He^+$ ,  $He^{++}$ , and  $e^-$ , as well as the five deuterium species D,  $D^+$ ,  $D^-$ , HD and  $HD^+$ . All relevant cooling mechanisms are included, i.e., H and He atomic line cooling, bremsstrahlung, inverse Compton scattering, and collisional excitation cooling via  $H_2$  and HD (Johnson & Bromm 2006).

In Figure 3, we show the hydrogen number density and metallicity averaged along the line of sight within the central  $\simeq 100$  kpc (comoving) at two different output times, from  $z \simeq 25$ , briefly after the first star-forming minihalo has collapsed, to  $z = 16.4$ , closer to the virialization of the first galaxy. The distribution of metals produced by the first SN explosion is highly inhomogeneous, and the metallicity can reach up to  $Z \sim 10^{-2.5}Z_\odot$ , which is already larger than any of the values discussed for the critical metallicity,  $Z_{\text{crit}} \lesssim 10^{-4}Z_\odot$  (e.g., Bromm et al. 2001a; Bromm & Loeb 2003; Frebel et al. 2007), including those predicted for a dust-driven Pop III/Pop II transition, where  $10^{-6}Z_\odot < Z_{\text{crit}} < 10^{-5}Z_\odot$  (Omukai et

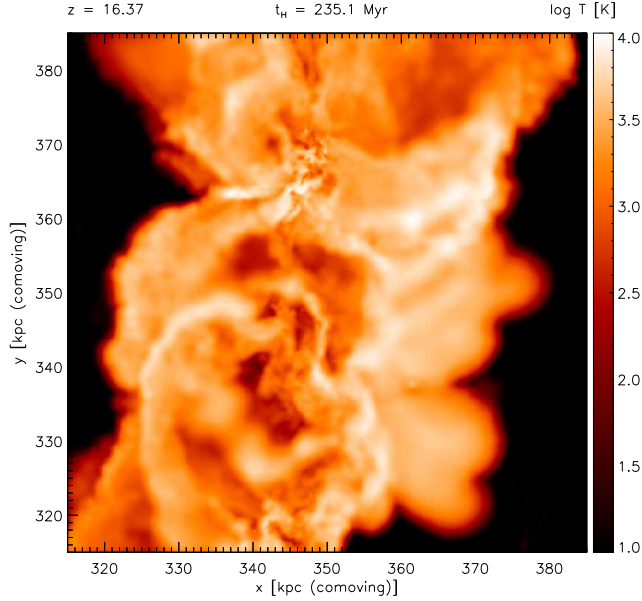


FIG. 4.— Environment for high- $z$  GRBs. Shown are temperature contours along the line of sight within the central  $\simeq 100$  kpc (comoving) at  $z = 16.4$ , corresponding to panel (b) in Fig. 3. The center of the growing galaxy is highly turbulent, with pockets of cold gas embedded in a hotter, diffuse medium.

al. 2005; Schneider et al. 2006). The implication is that both Pop III and Pop I/II stars will form during the assembly of the first galaxies (Johnson et al. 2008; Maio et al. 2010), in turn giving rise to the simultaneous occurrence of Pop III and normal GRBs at a given redshift (Bromm & Loeb 2006; de Souza et al. 2011). Here, we will focus on the case of a Pop III burst exploding in one of the (still metal-free) first galaxy progenitor minihalos at  $z \simeq 16.4$  (see Section 5). In Figure 4, we show the temperature distribution in the vicinity of the explosion site, allowing us to calculate (thermal) line broadening in a realistic fashion.

#### 4. POP III AFTERGLOW EMISSION

##### 4.1. Basic Physics

Our modeling of the GRB broad-band afterglow emission follows standard prescriptions, and we here only briefly summarize the basic physics involved (for general reviews, see Mészáros 2006; Zhang 2007). We specifically consider a relativistic shell ejected from the progenitor of a GRB (e.g., Kobayashi 2000). The shell has a rest mass of  $M_0$ , an observed thickness of  $\Delta_0$ , and exhibits an initial Lorentz factor of  $\Gamma_0 = E_{\text{iso}}/M_0 c^2$ , where  $E_{\text{iso}}$  is the isotropic-equivalent explosion energy. The interaction between the shell and the surrounding medium with a density of  $n_0$  produces a forward and a reverse shock. The shocks, in turn, accelerate electrons to high energies, distributed according to a power-law:  $dN(\gamma_e)/d\gamma_e \propto \gamma_e^{-p}$  for  $\gamma_e \geq \gamma_m$ , where  $\gamma_e$  is the internal Lorentz factor for the electrons. The minimum Lorentz factor is set by assuming that a fraction  $\epsilon_e$  of the post-shock energy is transferred to the electrons, resulting in:  $\gamma_m = \epsilon_e \gamma (\gamma_p/m_e)(p-2)/(p-1)$ , where  $\gamma \sim \Gamma_0$  is the Lorentz factor of the shocked fluid (e.g., Blandford & McKee 1976; Sari et al. 1998). If one also assumes that a fraction  $\epsilon_B$  of the post-shock energy is deposited

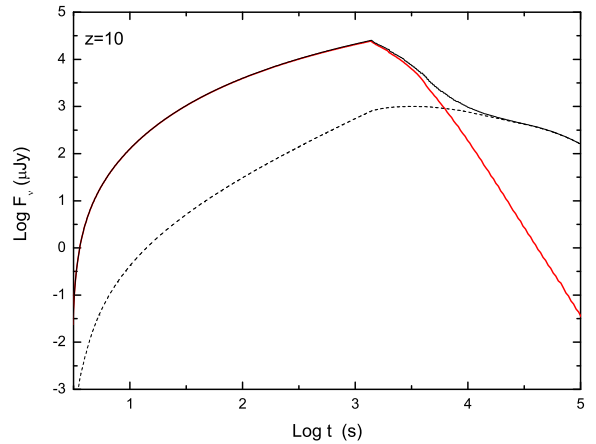


FIG. 5.— Flux density at  $\nu = 6.3 \times 10^{13}$  Hz (M band) as a function of observed time. We show the emission from the forward shock (dashed line), the reverse shock (solid red line), and their combination (solid black line). We use the parameters given in the text, for a GRB exploding in a minihalo with circumburst density  $n_0 = 0.5 \text{ cm}^{-3}$  at  $z = 10$ . It can be seen that the reverse shock dominates during the first few hours, reaching a brightness in excess of  $\sim 1$  mJy.

into random magnetic fields, the gyration of the shock-accelerated electrons around the magnetic field will generate synchrotron radiation, thus giving rise to the afterglow emission. There is then a second characteristic Lorentz factor,  $\gamma_c$ , determining the threshold below which electrons do not lose a significant fraction of their energy to radiation. Equating the synchrotron cooling time with the expansion time of the shell, one finds:  $\gamma_c m_e c^2 = P(\gamma_c) t_{\text{exp}}$ , where  $P(\gamma_e) = (4/3) \sigma_T c \gamma_e^2 (B^2/8\pi)$  is the synchrotron radiation power (Rybicki & Lightman 1979), and  $t_{\text{exp}}$  the expansion time, measured in the comoving fluid frame (Sari et al. 1998; Panaitescu & Kumar 2000). Therefore, the cooling Lorentz factor can be written as:  $\gamma_c = 6\pi m_e c / (\sigma_T B^2 t_{\text{exp}})$ .

For the resulting spectrum, there are now two cases: In the fast cooling case ( $\gamma_m > \gamma_c$ ), the flux can be calculated from

$$F_\nu = F_{\nu, \text{max}} \begin{cases} \left(\frac{\nu_a}{\nu_c}\right)^{1/3} \left(\frac{\nu}{\nu_a}\right)^2 & \nu < \nu_a \\ \left(\frac{\nu}{\nu_c}\right)^{1/3} & \nu_a < \nu < \nu_m \\ \left(\frac{\nu}{\nu_c}\right)^{-1/2} & \nu_c < \nu < \nu_m \\ \left(\frac{\nu_m}{\nu_c}\right)^{-1/2} \left(\frac{\nu}{\nu_m}\right)^{-p/2} & \nu_m < \nu, \end{cases}$$

whereas in the opposite, slow-cooling ( $\gamma_m < \gamma_c$ ), case, one has

$$F_\nu = F_{\nu, \text{max}} \begin{cases} \left(\frac{\nu_a}{\nu_m}\right)^{1/3} \left(\frac{\nu}{\nu_a}\right)^2 & \nu < \nu_a \\ \left(\frac{\nu}{\nu_m}\right)^{1/3} & \nu_a < \nu < \nu_m \\ \left(\frac{\nu}{\nu_m}\right)^{-(p-1)/2} & \nu_m < \nu < \nu_c \\ \left(\frac{\nu_c}{\nu_m}\right)^{-(p-1)/2} \left(\frac{\nu}{\nu_c}\right)^{-p/2} & \nu_c < \nu. \end{cases}$$

The break frequencies correspond to the electron Lorentz factors introduced above. The frequency  $\nu_a$  describes the onset of synchrotron self-absorption, which is important at low (radio) frequencies. The afterglow emission exhibits a different character before and after the reverse shock (RS) has crossed the shell. This

happens at a time  $t_{\oplus} \sim (1+z)\Delta_0/2c = 16.7\text{s}(1+z)\Delta_0/10^{12}\text{cm}$ , as measured in the observer frame. Before RS crossing ( $t < t_{\oplus}$ ), we have for the forward shock (“f”):

$$\begin{aligned}\nu_{m,f} &\propto (1+z)^{-1}\epsilon_e^2\epsilon_B^{1/2}\Delta_0^{-3/2}E_{\text{iso}}^{1/2}t^{-1}, \\ \nu_{c,f} &\propto (1+z)^{-1}\epsilon_B^{-3/2}n_0^{-1}\Delta_0^{-1/2}E_{\text{iso}}^{-1/2}t^{-1}, \\ \nu_{a,f} &\propto (1+z)^{-1}\epsilon_B^{6/5}n_0^{11/10}\Delta_0^{-1/2}E_{\text{iso}}^{7/10}t^{-2}, \\ F_{\nu,\text{max},f} &\propto (1+z)\epsilon_B^{1/2}n_0^{1/2}E_{\text{iso}}d_L^{-2}t, \quad (11)\end{aligned}$$

where  $d_L$  is the luminosity distance. Here and in the following we equate the pre-shock density with that established by photoionization-heating, at the time of the Pop III star’s death:  $n_0 \simeq n_{\text{pi}}$  (see Section 2). For the reverse shock (“r”), we have

$$\begin{aligned}\nu_{m,r} &\propto (1+z)^{-1}\epsilon_e^2\epsilon_B^{1/2}\Gamma_0^2n_0^{1/2}, \\ \nu_{c,r} &\propto (1+z)^{-1}\epsilon_B^{-3/2}n_0^{-1}\Delta_0^{-1/2}E_{\text{iso}}^{-1/2}t^{-1}, \\ \nu_{a,r} &\propto (1+z)^{-1}\epsilon_e^{6/13}\epsilon_B^{1/5}n_0^{1/5}\Gamma_0^{-8/5}\Delta_0^{-6/5}E_{\text{iso}}^{3/5}t^{-3/5}, \\ F_{\nu,\text{max},r} &\propto (1+z)\epsilon_B^{1/2}n_0^{1/4}\Gamma_0^{-1}\Delta_0^{-3/4}E_{\text{iso}}^{5/4}d_L^{-2}t^{1/2}. \quad (12)\end{aligned}$$

After RS crossing, we similarly have

$$\begin{aligned}\nu_{m,f} &= \nu_{m,f}(t_{\oplus}) \left(\frac{t}{t_{\oplus}}\right)^{-3/2}, \\ \nu_{c,f} &= \nu_{c,f}(t_{\oplus}) \left(\frac{t}{t_{\oplus}}\right)^{-1/2}, \\ \nu_{a,f} &= \nu_{a,f}(t_{\oplus}) \left(\frac{t}{t_{\oplus}}\right)^0, \\ F_{\nu,\text{max},f} &= F_{\nu,\text{max},f}(t_{\oplus}) \left(\frac{t}{t_{\oplus}}\right)^0, \quad (13)\end{aligned}$$

for the forward shock. For the reverse shock, we have

$$\begin{aligned}\nu_{m,r} &= \nu_{m,r}(t_{\oplus}) \left(\frac{t}{t_{\oplus}}\right)^{-3/2}, \\ \nu_{c,r} &= \nu_{c,r}(t_{\oplus}) \left(\frac{t}{t_{\oplus}}\right)^{-3/2}, \\ \nu_{a,r} &= \nu_{a,r}(t_{\oplus}) \left(\frac{t}{t_{\oplus}}\right)^{-1/2}, \\ F_{\nu,\text{max},r} &= F_{\nu,\text{max},r}(t_{\oplus}) \left(\frac{t}{t_{\oplus}}\right)^{-1}. \quad (14)\end{aligned}$$

The exact expressions, and further details, can be found in Kobayashi (2000) and Wu et al. (2003). Note that the latter study assumes the presence of a circumburst wind profile, whereas we here consider the constant-density (ISM) case, similar to Kobayashi (2000). The basic parameters of the afterglow emission region are:  $\Gamma_0 = 300$ ,  $E_{\text{iso}} = 10^{53}\text{erg}$ ,  $\Delta_0 = 10^{12}\text{cm}$ ,  $\epsilon_e = 0.3$ ,  $\epsilon_B = 0.1$ , and  $p = 2.5$ . We have verified that our afterglow predictions are consistent with those in Gou et al. (2004), and Inoue et al. (2007), as these papers focus on Pop III bursts at high redshifts as well. As an example, in Figure 5, we show the M-band light curve, corresponding to  $\nu = 6.3 \times 10^{13}\text{Hz}$ . It can be seen that the reverse shock

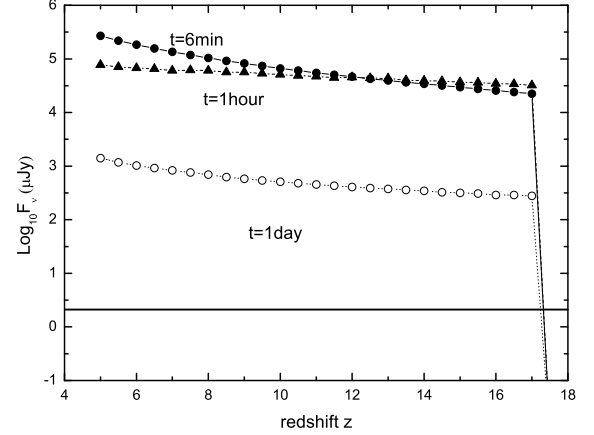


FIG. 6.— Observed flux at  $\nu = 1.36 \times 10^{14}\text{Hz}$  (K band) as a function of redshift. The lines indicate the flux at different observed times, as labelled. Here, we have assumed that the Pop III GRB is triggered in a minihalo environment, as modelled in Section 2.1. We mark the K-band sensitivity of the NIRSpect instrument on board the *JWST* with a horizontal line. The sharp cut-off at  $z \simeq 17$  is due to  $\text{Ly}\alpha$  absorption in the IGM.

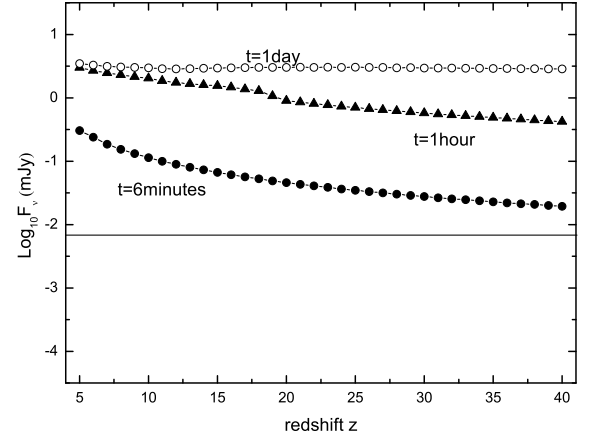


FIG. 7.— Observed radio flux (in mJy) at  $\nu = 5\text{GHz}$  as a function of redshift, again for a minihalo burst environment. We employ the same convention for the lines and symbols as in Fig. 6, but we now mark the corresponding sensitivity (*horizontal line*) for the EVLA. As is evident, the radio flux increases with observed time, and is well within reach of detection.

emission dominates during the first few hours, whereas the forward shock component takes over at later times.

#### 4.2. Redshift Dependence

We here briefly summarize the key aspects of afterglows triggered by Pop III stars. Figure 6 shows the observed flux at  $\nu = 1.36 \times 10^{14}\text{Hz}$  as a function of redshift for Pop III GRBs in a minihalo. According to Section 2.1, circumburst densities can then be written as  $n \simeq 1\text{cm}^{-3}(1+z)/20$ . The lines with filled dots, black triangles and open dots correspond to an observed time of 6 minutes, 1 hour and 1 day respectively. The straight



line marks the K-band sensitivity for the near-infrared spectrograph (NIRSpec) on *JWST*, estimated for a resolution of  $R = 1000$ , a signal-to-noise ratio of  $S/N = 10$ , and an integration time of 1 hour (Gardner et al. 2006). Once the observed frequency corresponds to an emitted frequency above the Ly $\alpha$  resonance,  $\nu_\alpha = 2.47 \times 10^{15}$  Hz, which occurs at  $z \simeq 17$  for the K-band, all flux will be completely absorbed by the intervening, still largely neutral IGM. As can be seen, in the *K* band the *JWST* will be able to detect GRBs, and to conduct spectroscopy on their afterglows, out to  $z \sim 16$  even after 1 day. In the *M* band, the redshift horizon is extended further still, to  $z \sim 35$ . At these frequencies, the afterglow flux is only weakly dependent on redshift. The main reason is that cosmic time dilation implies that a given observed time after the trigger corresponds to successively earlier emission times, where intrinsic afterglow luminosities are much brighter (Ciardi & Loeb 2000; Bromm & Loeb 2012). Secondly, circumburst densities modestly increase with redshift (see Section 2).

In Figure 7, we show the flux at  $\nu = 5$  GHz, again after  $t = 6$  minutes, 1 hour and 1 day. We calculate the sensitivity of the VLA, using the following expression (Ioka & Mészáros 2005)

$$F_\nu^{\text{sen}} = \frac{S/N \cdot 2k_B T_{\text{sys}}}{A_{\text{eff}} \sqrt{2t_{\text{int}} \Delta\nu}} \sim 23 \mu\text{Jy} \left( \frac{S/N}{5} \right) \left( \frac{t_{\text{int}}}{1 \text{ day}} \right)^{-1/2} \left( \frac{\Delta\nu}{50 \text{ MHz}} \right)^{-1/2} \quad (15)$$

where  $t_{\text{int}}$  is the integration time,  $\Delta\nu$  the bandwidth, and  $A_{\text{eff}}/T_{\text{sys}} \sim 2 \times 10^6 \text{ cm}^2 \text{ K}^{-1}$ . The bandwidth of the Expanded VLA (EVLA)<sup>1</sup> can be up to 8 GHz. For a 2 h integration in the 8 GHz band, the EVLA can thus reach a sensitivity of up to  $6.4 \mu\text{Jy}$ , which is shown as a horizontal line in Figure 7. We can see that the radio afterglows are easily within reach for the EVLA, up to  $z \sim 40$  (e.g., Chandra et al. 2010).

#### 4.2.1. Peak fluxes and wavelengths

According to hierarchical cosmic structure formation, the characteristic halo mass varies as a function of redshift. Thus, the typical observed peak flux and wavelength of Pop III GRBs are also a function of redshift. In the following, we derive ballpark estimates for these key quantities by considering  $2\sigma$  overdensities (e.g., figure 4 in Clarke & Bromm 2003). This provides us with the typical halo mass,  $M_{\text{vir}}$ , at a given redshift. In the  $2\sigma$  case, halo masses become less than  $10^5 M_\odot$  at redshift  $z > 15$ . Since this has dropped below the threshold mass for  $\text{H}_2$  cooling (e.g., Yoshida et al. 2003), Pop III stars could not form in such low-mass halos. For higher-sigma peaks, however, super-critical halos still exist at earlier times. Therefore, for simplicity we adopt  $M_{\text{vir}} = 10^5 M_\odot$  at  $z > 15$ . After the characteristic halo mass is thus determined, the virial temperature is fixed as well, and the ratio  $\epsilon \equiv (c_{s,i}/c_s)^2$  is known. The Shu solution then gives the circumburst densities at a given redshift (see Section 2), and GRB afterglow spectra can finally be calculated. Figure 8 shows the observed peak flux at observed time  $t = 6$  minutes, 1 hour and 1 day at  $z < 30$ .

<sup>1</sup> <http://www.aoc.nrao.edu/evla/>

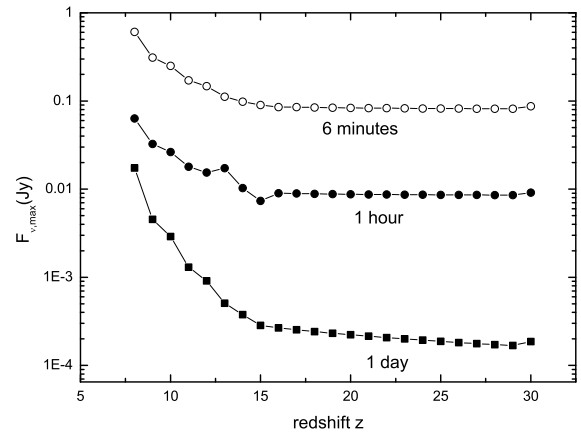


FIG. 8.— The observed maximum flux density as a function of redshift at different times,  $t = 1$  day, 1 hour and 6 minutes from bottom to top. We assume that the Pop III GRB has exploded in a minihalo. As can be seen, afterglow fluxes can reach substantial levels early on, and still remain at  $\sim$  mJy a day after the trigger, out to very high redshifts.

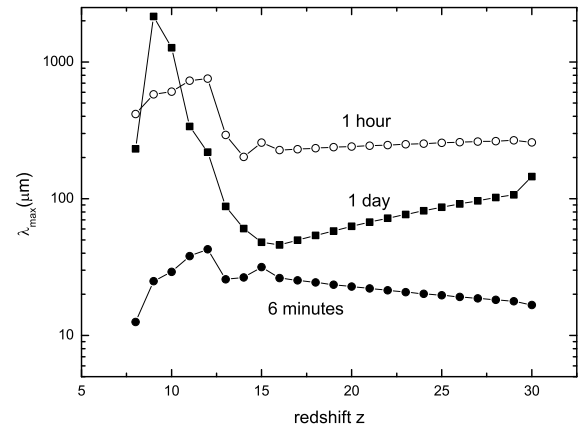


FIG. 9.— The observed maximum wavelength as a function of redshift at different times, as labelled, for a GRB exploding in a minihalo. The emission maxima range from mm to mid-IR wavelengths.

The peak flux varies from milli-Jansky to sub-Jansky. Figure 9 gives the observational peak wavelength at the same observed times for the same redshift range. The observed peak wavelengths vary from millimeter to mid-infrared bands. Early afterglows are best observed with facilities such as the *JWST*, or possibly adaptive-optics supported next-generation, extremely-large telescopes on the ground. At late times, radio facilities provide the optimal chance for detection. Among them is ALMA, which will allow to probe the afterglow in the mm and sub-mm regime, where the peak of the emission is located about 1 day after the explosion for  $z \sim 10$  sources.

## 5. METAL ABSORPTION LINES

As we have seen above, Pop III GRBs can in principle be detected out to very high redshifts. Their afterglow



spectra provide us with a unique probe into the state of the early IGM, including its degree of ionization (e.g., Totani et al. 2006) and metal enrichment. The latter will be encoded in absorption lines imprinted on the smooth afterglow emission with a signature that depends on the nature of the Pop III SNe. Here, we will consider for simplicity that prior to the GRB only one nearby SN exploded beforehand, dispersing its complement of heavy elements into the otherwise pristine IGM. Such a scenario is consistent with the clustered nature of Pop III star formation, as is expected for the high- $\sigma$  peak host systems (e.g., Greif & Bromm 2006). Specifically, we here explore nucleosynthetic yields for Type II core-collapse SNe, and for pair-instability supernovae (PISNe). In Table 1, we summarize the average yields per SN,  $Y_X$ , for select elements that are expected to dominate the spectral signature. For Type II SNe, we use the yields of Woosley & Weaver (1995). These depend on the explosion energy, which introduces uncertainties of  $\sim 25\%$ . For the PISN scenario, we utilize the yields of Heger & Woosley (2002; 2010). Table 1 also lists the properties of several key transitions, including their rest-frame wavelength,  $\lambda_i$ , and their oscillator strength,  $f_{\text{osc},i}$ .

We employ a simple model for the ionization structure of the metal-enriched gas. If the hydrogen in this region is substantially neutral, metals will reside in states typical of H I regions in the Milky Way (C II, O I, Si II, and Fe II for the elements of interest), because photons able to further ionize these elements will be absorbed by H I (Furlanetto & Loeb 2003). The ionization potential of O I is 13.62 eV, and it remains locked in charge exchange equilibrium with H I (Oh 2002). A modest extragalactic radiation background at frequencies below the Lyman limit could easily maintain these metals in a singly-ionized state (e.g., Furlanetto & Loeb 2003). We thus assume that C, O, Si, and Fe are predominantly in the ionization states typical for Galactic H I clouds.

### 5.1. Cosmological Radiative Transfer

Employing comoving coordinates, the equation of cosmological radiative transfer is (e.g., Abel et al. 1999):

$$\frac{1}{c} \frac{\partial I_\nu}{\partial t} + \frac{\hat{n} \cdot \nabla I_\nu}{\bar{a}} - \frac{H(t)}{c} (\nu \frac{\partial I_\nu}{\partial \nu} - 3I_\nu) = j_\nu - k_\nu I_\nu, \quad (16)$$

where  $I_\nu$  is the intensity of the radiation field,  $\hat{n}$  a unit vector along the direction of the ray,  $H(t) \equiv \dot{a}/a$  the Hubble constant<sup>2</sup>, and  $\bar{a} \equiv a(t+dt)/a(t)$  the ratio of cosmic scale factors separated by  $dt$ . Here  $j_\nu$  and  $k_\nu$  denote the emission and absorption coefficient, respectively. Equation (16) can be simplified if the effects of cosmic expansion are negligible. This will be the case if the light-crossing time,  $t_{\text{light}} = L/c$ , over the region of interest, here the (physical) size of our simulation box,  $L = 1 \text{ Mpc}/(1+z)$ , is small compared to the Hubble time,  $t_H \simeq 5 \times 10^8 \text{ yr} [(1+z)/10]^{-3/2}$ . Since  $t_{\text{light}} \ll t_H$ , the transfer equation reverts to its non-cosmological form:

$$\frac{1}{c} \frac{\partial I_\nu}{\partial t} + \hat{n} \cdot \nabla I_\nu = j_\nu - k_\nu I_\nu. \quad (17)$$

<sup>2</sup> We here employ the same cosmological parameters as in the underlying simulation (see Sec. 3).

We further neglect any diffuse (re-)emission of radiation, such that  $j_\nu = 0$ , and assume near steady-state conditions ( $\partial/\partial t \simeq 0$ ), resulting in the static transfer equation:

$$\hat{n} \cdot \nabla I_\nu = -k_\nu I_\nu. \quad (18)$$

If  $I_\nu(0)$  is the intensity of the central afterglow, approximately treated as a point source, we have the standard solution:  $I_\nu = I_\nu(0) \exp(-\tau_\nu)$ , where  $\tau_\nu$  is the optical depth along the line-of-sight (LOS).

We can obtain the optical depth as follows. For a (physical) differential distance element,  $dl$ , along the given LOS, we have:  $d\tau_\nu = \sigma_\nu n_X dl$ , where

$$\sigma_\nu = \sqrt{\pi} e^2 / (m_e c) f_{\text{osc},i} H(u, x) / \Delta\nu_D \quad (19)$$

is the frequency dependent absorption cross-section, and  $n_X$  the number density of species X (e.g., O I, C II, Fe II, Si II, H I). In the above equation,  $\Delta\nu_D \equiv b\nu_i/c$  is the Doppler width<sup>3</sup> with parameter  $b = \sqrt{2k_B T/m_H}$ . The Voigt function,  $H$ , is given by

$$H(u, x) = \frac{u}{\pi} \int_{-\infty}^{+\infty} \frac{e^{-y^2}}{(x-y)^2 + u^2} dy. \quad (20)$$

Here, the relative strength of natural (damping) to Doppler broadening is described by the parameter

$$u = \frac{\Gamma_i}{4\pi\Delta\nu_D}, \quad (21)$$

where  $\Gamma_i$  is the damping constant for transition  $i$  (Morton & Smith 1973). The variables  $x = (\nu - \nu_i)/\Delta\nu_D$  and  $y = v/b$  are the frequency difference relative to the line center in Doppler units, and the normalized particle velocity, with respect to the GRB location, respectively. The total LOS value of the optical depth is then:  $\tau_\nu = \int \sigma_\nu n_X dl$ . We note that we can neglect any wavelength differences between the GRB source and the metal absorber, because of the very small expansion-generated redshift on the scale of our simulation box. Specifically, we estimate that  $\Delta z = \Delta t / (7.5 \times 10^7 \text{ yr}) \sim 0.005$ , where we assume  $z \sim 10$ , and  $\Delta t \sim t_{\text{light}} \sim 3 \times 10^5 \text{ yr}$ .

We extract the optical depths along random lines of sight with the ray-tracing algorithm of Greif et al. (2009). We choose  $N_\theta = 160$  and  $N_\phi = 320$  in the spherical coordinates, which corresponds to 51200 rays. For each ray, we use 200 logarithmically-spaced radial bins, and approximate the optical depth integral with a sum along the LOS. The Pop III GRB will likely explode in a still substantially neutral IGM. Any flux shortward of the Ly $\alpha$  resonance is therefore completely absorbed, and because of the corresponding very large optical depth, there will be absorption in the red damping wing as well. We model this with the analytical formula given by Miralda-Escudé (1998), using  $z_{\text{reion}} = 7$  and standard cosmological parameters (Komatsu et al. 2011). The line shape is not very sensitive to the choice of  $z_{\text{reion}}$  (Bromm et al. 2001b).

### 5.2. Synthetic Spectra

<sup>3</sup> We here neglect any broadening from turbulent motions. This assumption is good in the minihalo progenitors, but breaks down in the emerging atomic cooling halo.

TABLE 1  
SUPERNOVA YIELDS AND IMPORTANT TRANSITIONS.

Element	$Y_X$ (Scalo) <sup>a</sup>	$Y_X$ (VMS) <sup>b</sup>	Ionization State	$\lambda_i$ (Å) <sup>c</sup>	$f_{osc,i}$ <sup>d</sup>
C	0.1 $M_\odot$	4.1 $M_\odot$	C II	1334.5	0.1278
			C IV	1548.2	0.1908
			C IV	1550.8	0.09522
O	0.5	44	O I	1302.2	0.04887
Si	0.06	16	Si II	1304.4	0.094
			Si IV	1393.8	0.514
			Si IV	1402.8	0.2553
			Fe II	1608.5	0.058
Fe	0.07	6.4	Fe II	2344.2	0.114
			Fe II	2382.8	0.300
			Fe II	2382.8	0.300

<sup>a</sup> Metal yield in Scalo IMF case.

<sup>b</sup> Metal yield in VMS IMF case.

<sup>c</sup> Rest-frame transition wavelength.

<sup>d</sup> Oscillator strength.

TABLE 2  
LINE FLUX RATIOS FROM MINIMUM TO MAXIMUM.

observed time IMF	crossing time VMS	crossing time Scalo	1 day VMS	1 day Scalo
O I/C II 1334.5Å	0.078-0.086	0.918-0.965	0.079-0.090	0.091-0.097
O I/Fe II 2334.2Å	0.014-0.030	0.408-0.444	0.014-0.042	0.040-0.043
O I/Fe II 2382.8Å	0.019-0.031	0.424-0.458	0.018-0.045	0.041-0.045
O I/Si II 1304.4Å	0.045-0.059	0.807-0.881	0.045-0.089	0.081-0.088
O I/Fe II 1608.5Å	0.078-0.090	0.800-0.852	0.078-0.105	0.080-0.085

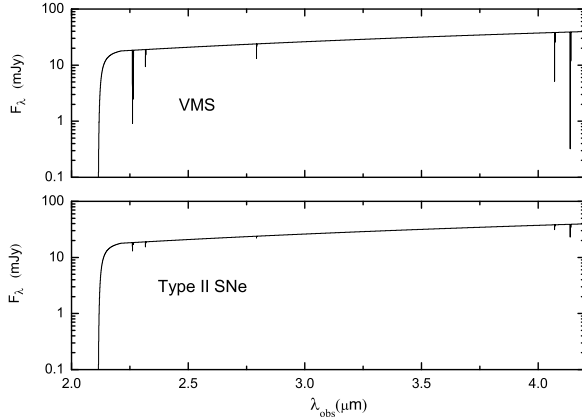


FIG. 10.— Total GRB spectrum observed at the reverse shock crossing time:  $t_\oplus = 16.7 \times (1 + 16.4)$  s. We show the spectral region redshifted into the near IR, accessible to the NIRCam and NIRSpect instruments on board the *JWST*. Metal absorption lines are imprinted according to the Pop III SN event, PISN vs. core-collapse (Type II). The former originates from a very massive star (VMS) progenitor, whereas the latter from a less massive one. In each case, the cutoff at short wavelengths is due to Lyman- $\alpha$  scattering in the neutral IGM.

In Figure 10, we show the part of the resulting afterglow spectrum that has been redshifted into the near-IR, where the *JWST* is most sensitive. For the two assumptions regarding the Pop III IMF, top-heavy (VMS) and more normal (Scalo), the spectra are depicted at the reverse shock crossing time. The metal absorption lines are imprinted on the smooth underlying GRB afterglow spectrum, rendering their identification straightforward. The cutoff at short wavelengths is due to Lyman- $\alpha$  scat-

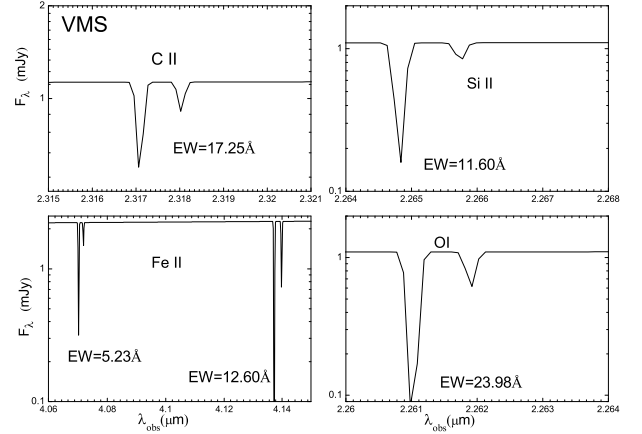


FIG. 11.— Spectral signature of metal absorption lines at the reverse shock crossing time:  $t_\oplus = 16.7 \times (1 + 16.4)$  s. We use the metal yields in the VMS case. The observed equivalent widths (EWs) are also shown in the figure. If multiple lines are present, the given EWs belong to the strongest lines in each panel.

tering in the IGM which is expected to be still completely neutral at  $z > 10$ . For detailed predictions, it is advantageous to quantify the strength of absorption lines through equivalent widths (EWs). The observed EWs can be calculated from

$$W = (1 + z) \int [1 - e^{-\tau(\lambda)}] d\lambda. \quad (22)$$

In Figures 11 and 12, we zoom in on the vicinity of the strongest lines, again at the reverse shock crossing time for both IMF cases. In addition, we explicitly give the derived EWs, which are about a few ten Å for a

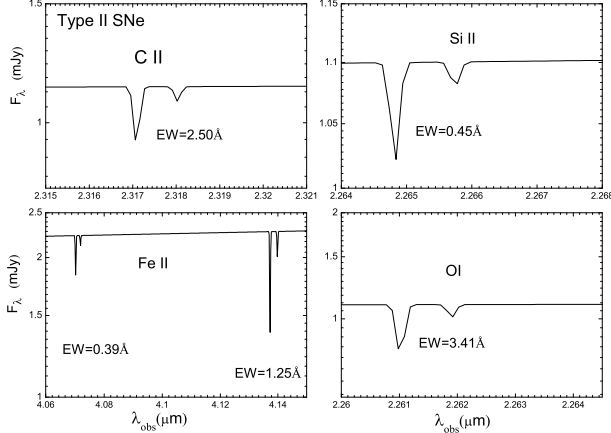


FIG. 12.— The same as Fig. 11, but displaying metal absorption lines for a normal (Scalo) Pop III IMF. Individual EWs are again given for the strongest lines in each panel.

top-heavy IMF, and an order of magnitude smaller for a normal (Scalo) IMF. The EW values do not change significantly, if evaluated at 1 day after the explosion. Such line strengths are well within reach of the NIRSpect instrument on board the *JWST*, which has a spectral resolution up to  $R \equiv \lambda/\Delta\lambda = 1000$ , and a line sensitivity of  $10^{-18} \text{ erg s}^{-1} \text{ cm}^{-2}$  (Gardner et al. 2006). In general, the limiting equivalent width of an unresolved line at observed wavelength  $\lambda_{\text{obs}}$ , at  $5\sigma$  significance, is (Tumlinson et al. 2002):

$$W_{\min} = \frac{5\lambda_{\text{obs}}}{R(S/N)}, \quad (23)$$

where  $S/N$  is the signal-to-noise ratio per resolution element. Within our assumptions, therefore, spectroscopy of Pop III GRB afterglows will be able to distinguish between different enrichment events, PISN vs. core-collapse. There is, however, a possible complication. The total enrichment level would be rather similar to that from one PISN for the case of 10 Type II SNe. Such a situation is not implausible, given the number of Pop III star formation sites, i.e., minihalos, in the vicinity of the Pop III GRB (see Sec. 3). However, we could then still discriminate between the cases using absorption line flux ratios, which remain quite different.

In Table 2, we list ranges for select flux ratios, as encountered along different LOSs. We consider the ratios  $O\text{ I}/X$ , where  $X$  denotes another species, at both the reverse shock crossing time and at 1 day after the explosion. In the former case, there is an order of magnitude difference between the two IMFs, allowing a robust identification. At later times, however, this clear-cut signature disappears again. In Figure 13, we show the cumulative EW distribution for 100 randomly selected sightlines at redshift  $z = 16.4$ . Again, the resulting distributions are quite different for the two IMF cases. It is, however, important to note that the statistical significance of this analysis is limited by the fact that it is based on only one simulation, and only one GRB afterglow. In reality, observations will sample multiple explosion sites with respective LOS distributions that sample many clouds at various evolutionary stages along the way. Our analysis

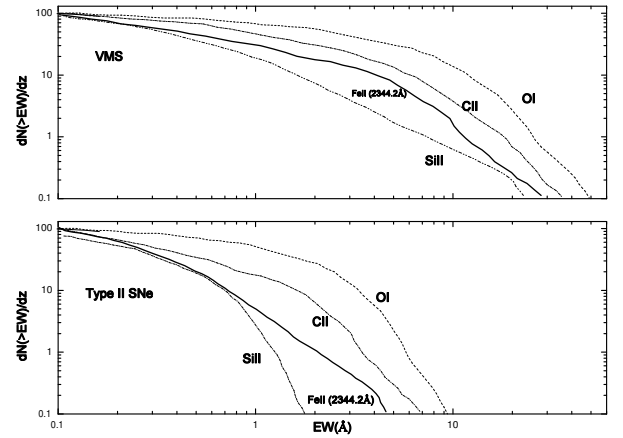


FIG. 13.— Cumulative distribution of metal line equivalent widths. The curves are calculated by tracing 100 randomly selected sightlines through the simulation box, centered on the location of the GRB. *Top panel:* VMS case. The curves show the main lines, as labelled. *Bottom panel:* Normal IMF case, corresponding to conventional core-collapse (Type II) SN explosions. It is evident that the resulting line statistics is quite distinct for the two IMF cases.

should still provide a representative view of the typical situation, whereas a more complete study has to await the further increase in available computational power.

## 6. SUMMARY AND CONCLUSIONS

In this paper, we develop a diagnostic to study pregalactic metal enrichment in the vicinity of the first galaxies. Specifically, we utilize the bright afterglow of a Pop III GRB as a featureless background source, and calculate the strength of metal absorption lines that are imprinted by the first heavy elements produced by Pop III SNe. To approximately derive the metal absorption line statistics, we use an existing highly-resolved simulation of the formation of a first galaxy which is characterized by the onset of atomic hydrogen cooling in a halo with virial temperature  $\gtrsim 10^4 \text{ K}$ . The reverse shock initially dominates the afterglow flux a few hours after explosion, followed by the forward shock emission later on. The fluxes in the near-IR and radio bands may be detectable with the *JWST* and the VLA out to  $z > 30$ . We predict that the afterglow emission peaks from near-IR to millimeter bands with peak fluxes from mJy to Jy at different observed times. Metal absorption lines in the GRB afterglow spectrum, giving rise to EWs of a few tens of Å, may allow us to distinguish whether the first heavy elements were produced in a Pop III star that died as a PISN, or a core-collapse SN. To this extent, the spectrum needs to be obtained sufficiently early, within the first few hours after the trigger.

The absorption signature of the first SN events might allow us to constrain the underlying mass scale of Pop III stars. This is the key input parameter to predict their evolution, nucleosynthetic yields, and modes of death, which in turn determine how the first stars impact subsequent cosmic history. The strength of the associated stellar feedback governs the assembly process of the first galaxies, in the sense that the stronger feedback from more massive stars shifts their formation to later stages

in the hierarchical build-up of structure (e.g., Ricotti et al. 2002; Greif et al. 2010; Frebel & Bromm 2012; Ritter et al. 2012; Wise et al. 2012).

It will, however, be very challenging to directly probe the initial epoch of cosmic star formation. The reason is that even the *JWST* will not be able to detect individual first stars, but instead only more massive stellar systems or clusters that form later on in more massive host systems (e.g., Pawlik et al. 2011). Pop III GRBs may thus afford us one of the few direct windows into the crucial epoch of first light, another one being the extremely energetic pair-instability SN or hypernova explosions that are predicted to end the lives of the most massive Pop III stars (e.g., Pan et al. 2012; Hummel et al. 2012). The promise provided by the combination of a wide field GRB trigger mission, such as JANUS or Lobster, with the next-generation of highly-sensitive near-

IR telescopes, such as the *JWST* or the planned ground-based extremely large facilities (the E-ELT<sup>4</sup>, GMT<sup>5</sup>, and TMT<sup>6</sup>), is huge. GRBs are likely to play a key role in finally opening up the high-redshift frontier, all the way back to the very beginning of star and black hole formation.

We are indebted to Anna Frebel and Steve Finkelstein for helpful discussions. This work is supported by the National Natural Science Foundation of China (grants 11103007 and 11033002). V. B. acknowledges support from NSF grant AST-1009928 and NASA ATFP grant NNX09AJ33G. K. S. C. is supported by the GRF Grants of the Government of the Hong Kong SAR under HKU 7011/09p. The simulations presented here were carried out at the Texas Advanced Computing Center (TACC).

## REFERENCES

- Abel, T., Norman, M. L., & Madau, P. 1999, *ApJ*, 523, 66
- Abel, T., Bryan, G. L., & Norman, M. L. 2002, *Science*, 295, 93
- Abel, T., Wise, J. H., & Bryan, G. L. 2007, *ApJ*, 659, L87
- Alvarez, M. A., Bromm, V., & Shapiro, P. R. 2006, *ApJ*, 639, 621
- Baraffe, I., Heger, A., & Woosley, S. E. 2001, *ApJ*, 550, 890
- Barkana, R. & Loeb, A. 2001, *Phys. Rep.*, 349, 125
- Barkana, R. & Loeb, A. 2004, *ApJ*, 601, 64
- Belczynski, K., Bulik, T., Heger, A., & Fryer, C. 2007, *ApJ*, 664, 986
- Blandford R. D., & McKee C. F. 1976, *Phys. Fluid*, 19, 1130
- Bloom, J. S. 2011, *What are Gamma-ray Bursts?* (Princeton: Princeton Univ. Press)
- Bromm, V., Coppi, P. S., & Larson, R. B. 1999, *ApJ*, 527, L5
- Bromm, V., Coppi, P. S., & Larson, R. B. 2002, *ApJ*, 564, 23
- Bromm, V., Ferrara, A., Coppi, P. S., & Larson, R. B. 2001a, *MNRAS*, 328, 969
- Bromm, V., Kudritzki, R. P., & Loeb, A. 2001b, *ApJ*, 552, 464
- Bromm, V., & Larson, R. B. 2004, *ARA&A*, 42, 79
- Bromm, V., & Loeb, A. 2002, *ApJ*, 575, 111
- Bromm, V., & Loeb, A. 2003, *Nature*, 425, 812
- Bromm, V., & Loeb, A. 2006, *ApJ*, 642, 382
- Bromm, V., & Loeb, A. 2012, in *Gamma-ray Bursts*, ed. C. Kouveliotou, S. E. Woosley & R. A. M. J. Wijers (Cambridge: Cambridge Univ. Press), arXiv:0706.2445v2
- Bromm, V., & Yoshida, N. 2011, *ARA&A*, 49, 373
- Bromm, V., Yoshida, N., Hernquist, L. & McKee, C. F. 2009, *Nature*, 459, 49
- Campisi, M. A., Maio, U., Salvaterra, R., & Ciardi, B. 2011, *MNRAS*, 416, 2760
- Cen, R. 2003, *ApJ*, 591, 12
- Chandra, P., et al. 2010, *ApJ*, 712, L31
- Chary, R., Berger E. & Cowie L. 2007, *ApJ* 671, 272
- Ciardi, B., & Loeb, A. 2000, *ApJ*, 540, 687
- Ciardi, B., & Ferrara, A. 2005, *Space Sci. Rev.*, 116, 625
- Clark, P. C., Glover, S. C. O., Klessen, R. S., & Bromm, V. 2011a, *ApJ*, 727, 110
- Clark, P. C., Glover, S. C. O., Smith, R. J., Greif, T. H., Klessen, R. S., & Bromm, V. 2011b, *Science*, 331, 1040
- Clarke, C. J., & Bromm, V. 2003, *MNRAS*, 343, 1224
- Cucchiara, A., et al. 2011, *ApJ*, 736, 7
- Dai, Z. G., Liang, E. W., & Xu, D. 2004, *ApJ*, 612, L101
- D’Elia, V., Campana, S., Covino, S., D’Avanzo, P., Piramonte, S., & Tagliaferri, G. 2011, *MNRAS*, 418, 680
- de Souza, R. S., Yoshida, N., & Ioka, K. 2011, *A&A*, 533, A32
- Elliott, J., Greiner, J., Khochfar, S., Schady, P., Johnson, J. L., & Rau, A. 2012, *A&A*, 539, A113
- Fan, X., Carilli, C. L., & Keating, B. 2006, *ARA&A*, 44, 415
- Frebel, A., Johnson, J. L., & Bromm, V. 2007, *MNRAS*, 380, L40
- Frebel, A., Johnson, J. L., & Bromm, V. 2009, *MNRAS*, 392, L50
- Frebel, A., & Bromm, V. 2012, *ApJ*, in press (arXiv:1010.1261)
- Furlanetto, S. R., & Loeb, A. 2003, *ApJ*, 588, 18
- Furlanetto, S. R., & Loeb, A. 2005, *ApJ*, 634, 1
- Gallerani, S., Salvaterra, R., Ferrara, A., & Choudhury, T. R. 2008, *MNRAS*, 388, L84
- Gardner, J. P., et al. 2006, *Space Sci. Rev.*, 123, 485
- Gou, L. J., Mészáros, P., Abel, T. & Zhang, B. 2004, *ApJ*, 604, 508
- Gou, L. J., Fox, D. B. & Mészáros, P. 2007, *ApJ*, 668, 1083
- Greif, T. H., & Bromm, V. 2006, *MNRAS*, 373, 128
- Greif, T. H., Johnson, J. L., Klessen, R. S. & Bromm, V. 2008, *MNRAS*, 387, 1021
- Greif, T. H., Johnson, J. L., Klessen, R. S. & Bromm, V. 2009, *MNRAS*, 399, 639
- Greif, T. H., Glover, S. C. O., Bromm, V., & Klessen, R. S. 2010, *ApJ*, 716, 510
- Greif, T. H., Springel, V., White, S. D. M., Glover, S. C. O., Clark, P. C., Smith, R. J., Klessen, R. S., & Bromm, V. 2011, *ApJ*, 737, 75
- Greif, T. H., Bromm, V., Clark, P. C., Glover, S. C. O., Smith, R. J., Klessen, R. S., Yoshida, N., & Springel, V. 2012, *MNRAS*, 424, 399
- Greiner, J., et al. 2009, *ApJ*, 693, 1610
- Haiman, Z., Thoul, A. A., & Loeb, A. 1996, *ApJ*, 464, 523
- Heger, A., & Woosley, S. E. 2002, *ApJ*, 567, 532
- Heger, A., & Woosley, S. E. 2010, *ApJ*, 724, 341
- Hjorth, J., et al. 2003, *Nature*, 423, 847
- Hosokawa, T., Omukai, K., Yoshida, N., & Yorke, H. W. 2011, *Science*, 334, 1250
- Hummel, J. A., Pawlik, A. H., Milosavljević, M., & Bromm, V. 2012, *ApJ*, in press (arXiv:1112.5207)
- Inoue, S., Omukai, K., & Ciardi, B. 2007, *MNRAS*, 380, 1715
- Ioka, K., & Mészáros, P. 2005, *ApJ*, 619, 684
- Johnson, J. L., & Bromm, V. 2006, *MNRAS*, 366, 247
- Johnson, J. L., Greif, T. H., & Bromm, V. 2008, *MNRAS*, 388, 26
- Johnson, J. L., Greif, T. H., Bromm, V., Klessen, R. S., & Ippolito, J. 2009, *MNRAS*, 399, 37
- Karlsson, T., Bromm, V., & Bland-Hawthorn, J. 2012, *Rev. Mod. Phys.*, in press (arXiv:1101.4024)
- Kitayama, T., Yoshida, N., Susa, H., & Umemura, M. 2004, *ApJ*, 613, 631
- Kobayashi, S. 2000, *ApJ*, 545, 807
- Komatsu, E., et al. 2011, *ApJS*, 192, 18
- Kudritzki, R. P. 2002, *ApJ*, 577, 389
- Komissarov, S. S., & Barkov, M. V. 2010, *MNRAS*, 402, L25
- Lamb, D. Q., & Reichart, D. E. 2000, *ApJ*, 536, 1
- Loeb, A. 2010, *How did the First Stars and Galaxies Form?* (Princeton: Princeton Univ. Press)
- MacFadyen, A. I., Woosley, S. E., & Heger, A. 2001, *ApJ*, 550, 410
- Mackey, J., Bromm, V., & Hernquist, L. 2003, *ApJ*, 586, 1
- Madau, P., Ferrara, A., & Rees, M. J. 2001, *ApJ*, 555, 92

<sup>4</sup> <http://www.eso.org/sci/facilities/eelt/>

<sup>5</sup> <http://http://www.gmto.org/>

<sup>6</sup> <http://http://www.tmt.org/>

- Maio, U., Ciardi, B., Dolag, K., Tornatore, L., & Khochfar, S. 2010, *MNRAS*, 407, 1003
- McKee, C. F., & Tan, J. C. 2008, *ApJ*, 681, 771
- Mészáros, P. 2006, *Rep. Prog. Phys.*, 69, 2259
- Mészáros, P. & Ress, M. J. 2010, *ApJ*, 715, 967
- Miralda-Escudé, J. 1998, *ApJ*, 501, 15
- Morton, D. C., & Smith, W. H. 1973, *ApJS*, 26, 333
- Oh, S. P. 2002, *MNRAS*, 336, 1021
- Oh, S. P., & Haiman, Z. 2002, *ApJ*, 569, 558
- Omukai, K., Tsuribe, T., Schneider, R., & Ferrara, A. 2005, *ApJ*, 626, 627
- Oppenheimer, B. D., Davé, R., & Finlator, K. 2009, *MNRAS*, 396, 729
- Pan, T., Kasen, D., & Loeb, A. 2012, *MNRAS*, 422, 2701
- Panaiteescu, A., & Kumar, K. 2000, *ApJ*, 543, 66
- Pawlik, A. H., Milosavljević, M., & Bromm, V. 2011, *ApJ*, 731, 54
- Porciani, C., & Madau, P. 2001, *ApJ*, 548, 522
- Qian, Y. Z., & Wasserburg, G. J. 2001, *ApJ*, 559, 925
- Ricotti, M., Gnedin, N. Y., & Shull, J. M. 2002, *ApJ*, 575, 33
- Ritter, J. S., Safrank-Shrader, C., Gnat, O., Milosavljević, M., & Bromm, V. 2012, *ApJ*, submitted (arXiv:1203.2957)
- Rybicki, G. B., & Lightman, A. P. 1979, *Radiative Processes in Astrophysics* (New York: Wiley)
- Safrank-Shrader, C., Bromm, V., & Milosavljević, M. 2010, *ApJ*, 723, 1568
- Safrank-Shrader, C., Agarwal, M., Federrath, C., Dubey, A., Milosavljević, M., & Bromm, V. 2012, *MNRAS*, submitted (arXiv:1205.3835)
- Salvaterra, R., et al. 2009, *Nature*, 461, 1258
- Sari R., Piran T., & Narayan R. 1998, *ApJ*, 497, L17
- Schneider, R., Ferrara, A., Natarajan, P., & Omukai, K. 2002, *ApJ*, 571, 30
- Schneider, R., Omukai, K., Inoue, A. K., & Ferrara, A. 2006, *MNRAS*, 369, 1437
- Shu, F. H., Lizano, S., Galli, D., Cantó, J., & Laughlin, G. 2002, *ApJ*, 580, 969
- Smith, R. J., Glover, S. C. O., Clark, P. C., Greif, T. H., & Klessen, R. S. 2011, *MNRAS*, 414, 3633
- Spergel, D. N., et al. 2003, *ApJS*, 148, 175
- Stacy, A., Greif, T. H., & Bromm, V. 2010, *MNRAS*, 403, 45
- Stacy, A., Bromm, V., & Loeb, A. 2011, *MNRAS*, 413, 543
- Stacy, A., Greif, T. H., & Bromm, V. 2012, *MNRAS*, 422, 290
- Stanek, K. Z., et al. 2003, *ApJ*, 591, L17
- Suwa, Y., & Ioka, K. 2011, *ApJ*, 726, 107
- Tanvir, N. R., et al. 2009, *Nature*, 461, 1254
- Tegmark, M., Silk, J., Rees, M. J., Blanchard, A., Abel, T., & Palla, F. 1997, *ApJ*, 474, 1
- Toma, K., Sakamoto, T. & Mészáros, P. 2011, *ApJ*, 731, 127
- Tornatore, L., Ferrara, A. & Schneider, R. 2007, *MNRAS*, 382, 945
- Totani, T. 1997, *ApJ*, 486, L71
- Totani, T., et al. 2006, *PASJ*, 58, 485
- Tumlinson, J., et al. 2002, *ApJ*, 566, 857
- Tumlinson, J. 2010, *ApJ*, 708, 1398
- Wang, F. Y. & Dai, Z. G. 2009, *MNRAS*, 400, L10
- Wang, F. Y. & Dai, Z. G. 2011, *ApJ*, 727, L34
- Wang, F. Y., Qi, S. & Dai, Z. G. 2011, *MNRAS*, 415, 3423
- Whalen, D., Abel, T., & Norman, M. L. 2004, *ApJ*, 610, 14
- Wijers, R. A. M. J., Bloom, J. S., Bagla, J. S., & Natarajan, P. 1998, *MNRAS*, 294, L13
- Wise, J. H., & Abel, T. 2007, *ApJ*, 665, 899
- Wise, J. H., & Abel, T. 2008, *ApJ*, 685, 40
- Wise, J. H., Turk, M. J., Norman, M. L., & Abel, T. 2012, *ApJ*, 745, 50
- Woosley, S. E. 1993, *ApJ*, 405, 273
- Woosley, S. E. & Bloom, J. S. 2006, *ARA&A*, 44, 507
- Woosley, S. E., & Weaver, T. A. 1995, *ApJS*, 101, 181
- Wu, X. F., Dai, Z. G., Huang, Y. F., & Lu, T. 2003, *MNRAS*, 342, 1131
- Wyithe, J. S. B., & Loeb, A. 2003, *ApJ*, 586, 693
- Yoshida, N., Abel, T., Hernquist, L., Sugiyama, N. 2003, *ApJ*, 592, 645
- Yüksel, H. et al. 2008, *ApJ*, 683, L5
- Zhang, B. 2007, *Chin. J. Astron. Astrophys.*, 7, 1
- Zhang, B., et al. 2009, *ApJ*, 703, 1696